Journal of Nuclear Materials 605 (2025) 155558

Contents lists available at ScienceDirect

Journal of Nuclear Materials

journal homepage: www.elsevier.com/locate/jnucmat

Correlation of mechanics degradation and thermal aging damage defects in Z3CN20.09M cast austenitic stainless steels

Chao Ye [a,b,*], Ni Jiang [a,b], Jiannan Hao [c], Xinjie Ma [c], Huiping Liu [a,b], Jiao Luo [b], Penghui Lei [d], Fangjie Shi [e], Qianwu Li [e], Yuhua Hang [e], Pan Qi [f], Qing Peng [c,g,h,*]

[a] Institute of Clean Energy, Yangtze River Delta Research Institute, Northwestern Polytechnical University, Taicang 215400, China
[b] School of Materials Science and Engineering, Northwestern Polytechnical University, Xi'an 710072, China
[c] State Key Laboratory of Nonlinear Mechanics, Institute of Mechanics, Chinese Academy of Sciences, Beijing 100190, PR China
[d] School of Nuclear Science and Technology, Xi'an Jiaotong University, Xi'an, PR China
[e] Suzhou Nuclear Power Research Institute, Suzhou 215004, China
[f] China Nuclear Power Operation Technology Corporation, LTD, Wuhan, 430223, China
[g] Center of Materials Science and Optoelectronics Engineering, University of Chinese Academy of Sciences, Beijing 100049, China
[h] Guangdong Aerospace Research Academy, Guangzhou 511458, China

HIGHLIGHTS

- 400℃ thermally aged Z3CN20.09 M steels were characterized and tested.
- A quantitative model related with aging defects and mechanical properties is set.
- Impact energy and Cr segregation are chosen as the characteristic parameters.

GRAPHICAL ABSTRACT

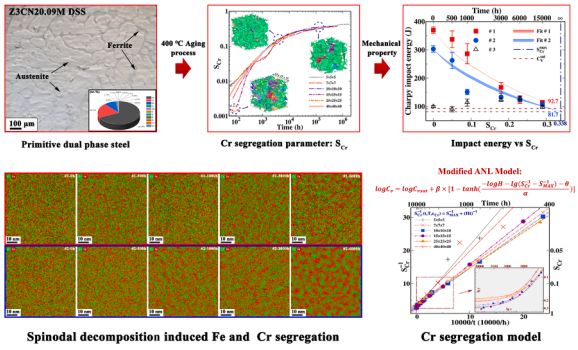

ARTICLE INFO

Keywords:
Z3CN20.09M CASSs
Thermal aging defect
Charpy impact energy
Quantitative mechanical model

ABSTRACT

Microstructural characterization and mechanical testing were performed on 400℃ thermally aged Z3CN20.09 M cast austenitic stainless steels. A quantitative mathematical model was introduced for the relationship between aging defects and mechanical properties. Charpy impact energy was used as a characteristic mechanical parameter, and the short-range order of the Cr element segregation that induced by spinodal decomposition was chosen as the characteristic defect parameter. The macroscopic mechanical properties and the microscopic thermal aging defects were quantitatively correlated in this model, which has a great reference significance in safety assessment and lifetime prediction of the reactor structural materials.

* Corresponding authors.
E-mail addresses: yechao@nwpu.edu.cn (C. Ye), pengqing@imech.ac.cn (Q. Peng).

https://doi.org/10.1016/j.jnucmat.2024.155558
Received 12 September 2024; Received in revised form 1 December 2024; Accepted 2 December 2024
Available online 3 December 2024

1. Introduction

As one of the nuclear safety components with the first level in reactors, the operating conditions of the primary pipes in the first circuit are very severe, including high temperature, high pressure, and corrosive environment. In addition to the perfect mechanical properties [1,2] (sufficient strength, high plasticity and toughness, good fatigue resistance, ease of processing, and welding performance), the primary pipe material also requires resistance to thermal aging effect [3,4] and high-pressure water corrosion [5,6]. Most early nuclear power plant primary circuit pipelines were made of 304 austenitic stainless steel (corresponding cast steel is CF-8) [7]. Later, in an effort to improve the high-temperature and high-pressure intergranular stress corrosion resistance, 316 stainless steel with the component of 2 %~3 % Mo (corresponding cast steel is CF-8 M) was gradually used [8]. In recent decades, United States and Japan have developed nuclear grade nitrogen controlled 316 L stainless steel, while France has invested heavily in a series of research on austenitic stainless-steel materials, developing Z2CND18.12 and Z3CN20.09 M primary pipeline materials [9–11]. Wherein, Z3CN20.09 M cast austenitic stainless steels (CASSs) with a dual phase structure (approximately 5 %~20 % ferrite distributed in an island-like manner in the austenite matrix) can meet the service performance well and is widely used as the main pipeline in the primary circuit of nuclear power plants [12].

The Z3CN20.09 M CASS has been safely served in Daya Bay nuclear plant for about 30 years in China, which is close to the design lifetime 40 years of reactors and has reached half of the design lifespan 60 years of the main pipeline [1]. During a long period of service in reactors, thermal aging embrittlement (TAE) is prone to occur in the Z3CN20.09 M CASS, which is mainly related with the spinodal decomposition in ferrite phase [13]. Generally, at the operating temperature of the reactor, the thermal aging process proceeds very slowly. As the thermal aging process of primary coolant pipe at the 300 °C operating temperature is very slow, accelerated thermal aging experiments at 400 ℃ are customarily performed for laboratory researches. [14]. Therefore, most researches about the thermal aging effects are based on the results of the accelerated experiments at 400 ℃ [14–20].

During the spinodal decomposition process, the α'+α domains (Cr-rich α' phases distribute in the Fe-rich α matrix phases) are generated at early stage due to the nanoscale segregation of Cr and Fe elements in ferrite. The lattice parameters of α' and α are very close and the lattice structures of them are both body-centered-cubic (BCC) [14,16,17]. While the slight lattice mismatch between α' and α phases can lead to an internal coherency strain, resulting in an increase of hardness and a decrease of toughness of ferrite phase [21]. On the other hand, the G-phase precipitates with the face-centered-cubic (FCC) structure are usually formed at the later stage of the thermal aging process [14]. It is generally believed that the precipitation of $Mn_6Ni_{16}Si_7$ G phase occurs through a two-step mechanism [22]: (1) Mn-Ni-Si solute clusters nucleation: enrichment of the elements at the α/α' and ferrite/austenite interfaces or along the dislocations by diffusion [4,17,23]; (2) G-phase nucleation: clusters grow to become a critical size first and then the solute within the cluster is further enriched and becomes a key component ($Ni_{16}Si_{3.5}Mn_6$) with a critical size of about 2.6 nm [24]. In addition, as the Cr/Ti can substitute to Mn sites and Fe/Mo can replace the Ni sites, the stoichiometric component of G-phase is quite complex [14].

For the practical application of CASS in reactors, the deterioration problem of the mechanical properties is always the key concern. In the past decades, the practical servicing experiences in reactors and the fundamental researches in laboratories proved that due to the changes of the microstructure and compositions in matrix phases of CASSs[25]. In addition to the Cr-rich α'-phase and G-phase, equilibrium thermodynamic calculation results of Byun et al. indicates that there are also many other minor phases might be formed commonly in both matrix phases during the thermal aging process, including σ-phase, chromium nitride (Cr_2N), Laves (η) phase, $M_{23}C_6$ carbide and π-phase [26]. Thermal aging can significantly lead to the deterioration of mechanical properties [27,28], including the increase in hardness and tensile strength, a decrease in ductility, Charpy impact energy and fracture toughness as the aging time go on. The deterioration degree of the mechanical properties of CASSs depends on the casting method, chemical properties, and the duration of exposure to working temperatures favorable for the embrittlement process [29]. Overall, amounts of in-depth researches have been conducted for the thermal aging of the CASS since 1900s [30–32]. The mechanisms of the influence of thermal aging on the microstructure damage and mechanical degradation of CASS are currently very clear. As early commercial nuclear power plants are approaching their design life, the issue of extending the life of reactors has received increasing attention, mainly related to the extension of the life of irreplaceable equipment such as primary coolant pipelines, reactor vessel internals, and other reactor pressure vessels typically made of CASS.

In this instance, besides the qualitative understanding of the thermal aging mechanisms, it is important to understand the quantitative relationship between the degree of thermal aging damage and the deterioration of mechanical properties, and then establish relevant mathematical models to predict the performance degradation status of the nuclear structural components. Based on extensive experimental and engineering data, researchers from the Argonne National Laboratory (ANL) completed a research program in assessing the thermal aging induced mechanical property degradation of cast stainless steels. They developed a comprehensive database of material properties and a fracture toughness estimation program by correlating data for thermally aged CASS samples [33,34]. However, there is still a lack of quantitative evaluation models related to the thermal aging damage characteristic defects. Hereby, taking the Z3CN20.09 M CASS as the research object, we attempt to identify the thermal aging damage characteristic defects closely related to the deterioration of mechanical properties and finally establish a quantitative mathematical model for these three parameters.

2. Materials and methods

Two kinds of Z3CN20.09 M cast austenitic stainless steels (#1–Made in France and #2–Made in China) have been researched for years. The focus is on the microstructural evolution and mechanical property degradation caused by thermal aging process. The elemental compositions of these two Z3CN20.09 M CASS samples are shown in the Table 1. And the structures of them are presented in Fig. 1(a). The lattice structures of the ferrite (F) and austenite (A) regions in Z3CN20.09 M CASS are BCC and FCC, respectively, as shown in the diffraction patterns inserted in Fig. 1(b). The compositional differences between these two phases mainly focus on the Cr element content, as shown in Fig. 1(c). During the accelerated thermal aging process, two large steel bulks were aged in two large muffle furnaces at 400 ℃ for 0 h ~ 6000 h, respectively. UDIAN programmable controllers equipped with K-type thermocouples was used to control the chamber temperatures, with an accuracy of $<\pm1$ ℃ and the spatial temperature variation of ±5 ℃. After varying thermal aging times, small pieces were cut from the large thermal aging Z3CN20.09 M CASS bulks for later characterization testing.

According to the Arrhenius equation as below, which was verified through extensive engineering practice by researchers and proposed by the U.S.NRC (United States Nuclear Regulatory Commission), the aging temperature and aging time used in this study can be equivalent to the material service temperature and service time in the typical reactor environment [35].

$$\frac{t_1}{t_2} = exp\left[\frac{E_a}{R}\left(\frac{1}{T_1}-\frac{1}{T_2}\right)\right] \quad (1)$$

where t_1 and t_2 are the service times corresponding to the service

Table 1
Chemical composition of #1 and #2 Z3CN20.09 M CASSs (wt%).

Ele.	Cr	Mo	Si	Ni	Mn	N	C	Cr	Fe
#1	20.893	0.103	1.020	9.760	1.058	0.045	0.026	20.893	Bal.
#2	20.238	0.060	1.183	8.885	1.108	0.026	0.035	20.238	Bal.

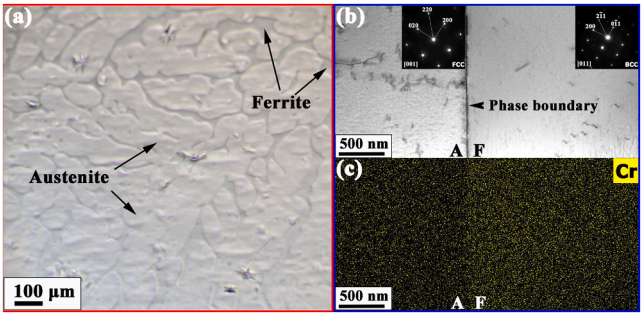

Fig. 1. (a) Surface morphology of the Z3CN20.09 M cast austenitic stainless steel and its chemical composition (wt%); (b) STEM image of the #1 sample and (c) the corresponding EDS mapping result of the Cr element.

temperatures T_1 and T_2 respectively; E_a is the activation energy of aging, usually taken as 100 kJ/mol [36]; R is the gas constant 8.314 $J/(mol{\cdot}K)$. Thus, a research sample aged for 3000 h at 400 ℃ is essentially equivalent to a sample aged for 7 years at the actual reactor operating temperature of 300 ℃.

According to the Chins Standard-GB/T 228.1–2021 Method B, a universal testing machine (AG-IC, SHIMADZU, Japan) with 100 kN capacity was used to perform the true stress tensile tests at room temperature. The gage scale pf the plate-type tensile specimens is 25 mm×6 mm×1 mm, and the tensile test was conducted two times for each datum point. The impact tests were conducted by using the Zwick RKP 450 pendulum impact testing machine at room temperature, thermal aging samples were processed into standard Charpy V-notch impact specimens. The instrumented testing method of Charpy V-notch pendulum impact test was adopted, and the impact curves were recorded throughout the process for subsequent analysis. The thermoelectric potential tests for the Z3CN20.09 M CASS block samples with the size of the test sample is 90×35×10 mm^3 were performed by a self-developed four-point thermoelectric potential equipment and the test results were the relative values to the thermoelectric potential of the copper. Each sample was polished by the #500~4000 SiC sandpapers to ensure consistent surface roughness.

The surface morphology of the thermal aged Z3CN20.09 M CASS samples were observed by using a scanning electron microscopy (SEM, ZEISS Gemini 2, Germany). TEM specimens with thicknesses <100 nm were prepared by a focused ion beam (FIB) technique. Aberration-corrected transmission electron microscopes (TEM, JEOL JEM-F200 and JEM-2100F) equipped with the configuration of the selected area electron diffraction (SAED) and energy dispersive X-ray spectroscopy (EDX) functions were used to observe the internal microstructures, phase structures and elementary composition evolutions of the thermal aged Z3CN20.09 M CASS TEM samples.

To explore the relationship between the microstructure of spinodal decomposition and the thermal aging process, the evolution of the atomistic phase separation is simulated by using the Monte Carlo (MC) method to simulate the evolution. We employ the Fe-Cr EAM potential developed by Bonny et al. [37] and utilize the LAMMPS code [38] to build a series of BCC Fe-Cr alloys and perform MC simulation, including simulation boxes ranging from 5 × 5 × 5 to 40×40×40 a_0^3 (a_0 is the lattice constant). Based on the Metropolis algorithm [39], a random exchange of vacancies with surrounding atoms is performed, and the total energy of the new configuration is calculated, whether to accept the new configuration is judged by the probability,

$$p = \begin{cases} 1, & \text{if } \Delta E \le 0, \\ \exp\left(-\dfrac{\Delta E}{kT}\right), & \text{otherwise}, \end{cases} \tag{2}$$

where ΔE is the energy difference of the exchanged system to the original one; k is the Boltzmann constant, and T is the temperature. Thereafter, a random number r, between 0 and 1, is chosen compared with p. While $r \le p$, the new configuration is accepted. To estimate the real aging time, the timestep for each atomic exchange is calculated by the residence-time algorithm [40],

$$\Delta t = -\frac{\ln r'}{\sum \Gamma_i}, \tag{3}$$

where $\sum \Gamma_i$ is the total frequency of a vacancy jumping into all its nearest-neighbor sites (8 in BCC lattice); Γ_i is calculated by Arrhenius's equation based on the migration energy barrier and the temperature [41], and r' is another randomly chosen number ranging from 0 to 1. The attempt frequency for the vacancy is 10^{13} /s, and the migration barriers of vacancy diffusion in this work is averagely set to be 0.6 eV [42,43] in consideration that most of the jumping occurred via the Fe atoms based on previous calculations.

3. Results

The results of macro-mechanical tests are shown in the following Fig. 2. The changes of Charpy impact energy of #1 and #2 Z3CN20.09 M CASS alloys with the increasing thermal aging time are exhibited in Fig. 2(a), which indicates that the impact energy of both shows an exponential downward trend and the Charpy impact energy of #2 sample decreased faster than that of #1 sample, and both tend to stabilize after 6000 h of thermal aging. Fig. 2(b) shows the evolutions of the tensile strength of the #1 and #2 samples with the change of thermal aging time, which clearly shows that the tensile strength of the #1 sample shows an exponential upward trend and tend to be stable after 6000 h of thermal aging. On the other hand, the tensile strength of the #2 sample increased rapidly in the early stage of the thermal aging process, while a turning point occurred, and it converted into a downward trend after being aged for ~3000 h

The fracture morphologies of the Z3CN20.09 M samples after tensile testing are shown in Fig. 3. Generally, with the increasing of thermal aging time, the fracture morphology of both #1 and #2 samples shows a trend from ductile fracture to brittle fracture, but there are still slight differences between them. Under the original state, the cross-section of #1 sample exhibits small-sized dimples with high density (Fig. 3a), while the density of dimples on the cross-section of #2 is lower than that of #1. In addition, Fig. 3(d) displays that there are many regions with the brittle fracture morphology on the cross-section of #2, which indicates that #1 has better toughness than #2 and it is consistent with the Charpy impact energy results in Fig. 2(a). After aging at 400 ℃ for 500 h, the quantity density of dimples decreases sharply, and only a few large-sized dimples can be observed on the cross-section of #1 and #2 samples, as shown in the Fig. 3(b) and (e). When the thermal aging time reaches 3000 h, the cross-sections of #1 and #2 samples show obvious brittle dissociation morphologies, as shown in the Fig. 3(c) and (f). Compared with #2, the ductile brittle transition process of #1 is more significant.

Some research results [44,45] indicate that the mechanical

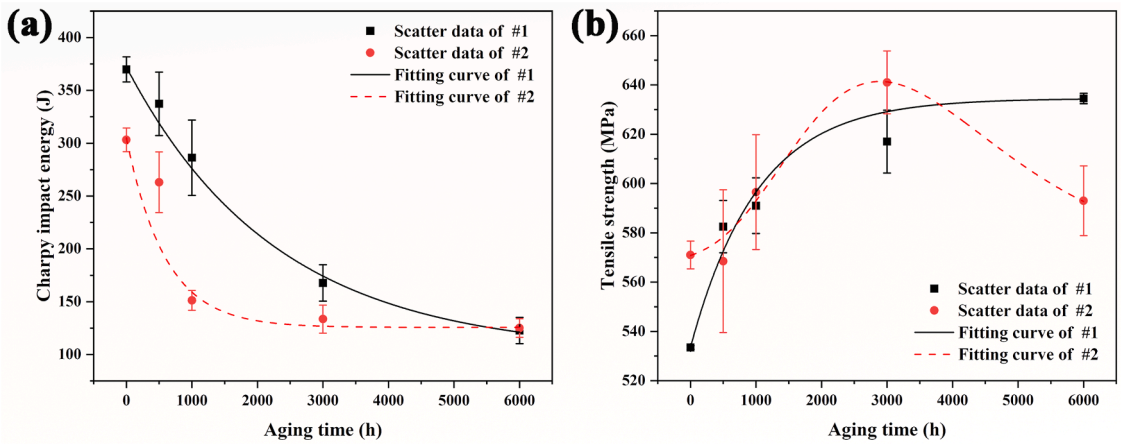

Fig. 2. Macro-mechanical properties of #1 and #2 Z3CN20.09 M CASS alloys under 0 ~ 6000 h thermal aging times: (a) Charpy impact energy; (b) Tensile strength. The curves in the figures are the trend fitting curves for the scatter mechanical data.

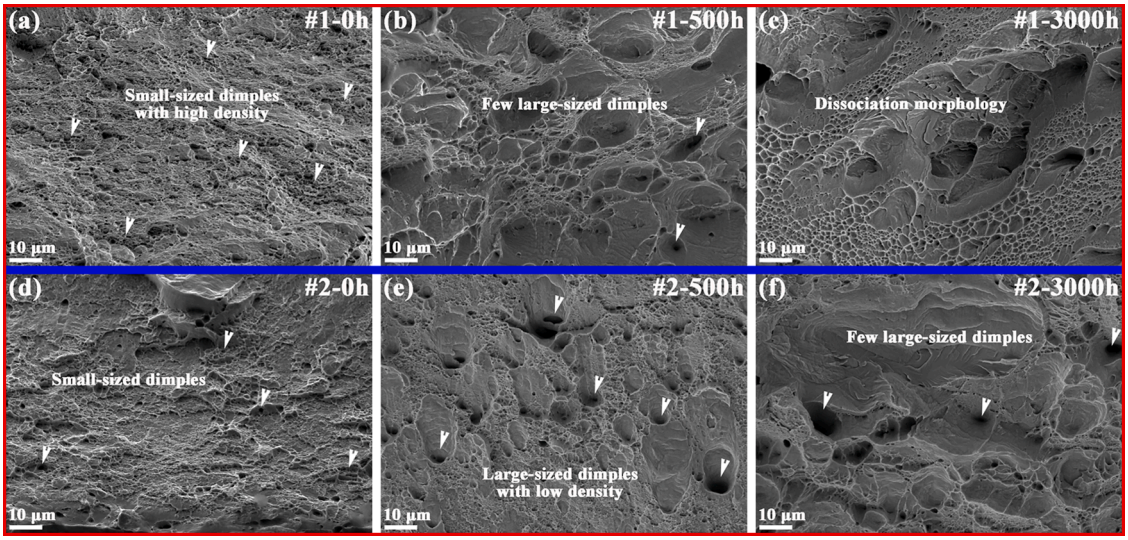

Fig. 3. Fracture morphology photos of #1 and #2 tensile Z3CN20.09 M CASS samples under different 400 ℃ thermal aging times: (a) #1, 0 h; (b) #1, 500 h; (c) #1, 3000 h; (d) #2, 0 h; (e) #2, 500 h; (f) #2, 3000 h

properties of the dual phase steel are mainly influenced by the hard ferrite phase. The overview STEM images of the evolution of dislocation structure in the Z3CN20.09 M samples are shown in Fig. 4. It can be clearly seen that the size and quantity of dislocations in the ferrite region of the original state #1 sample are small, and the defects in the ferrite region are less than those in the austenite region. On the contrary, the density and size of dislocations in the ferrite region of the #2 sample in the original state are significantly higher than those of the # 1 sample; After 1000 h of thermal aging, the size and density of dislocation defects inside the ferrite in samples #1 and #2 both show a downward trend; After 6000 h of thermal aging, the densities of dislocation defects in the ferrite of #1 and #2 both show a decrease trend. It is a common understanding that the increase in dislocation density could result in a decrease in material toughness, which indicates that the dislocation changes induced by thermal aging process inside the dual phase steel sample is not the main reason for the decrease in material mechanical properties [1].

Besides, the EDS mapping results of the Cr element inside the ferrite phase in the samples aged at different times are shown in Fig. 5. The green areas represent the aggregation of Cr atoms, and the red areas represent the aggregation of Fe atoms. For the #1 sample, the segregation of Cr element is not significant during the thermal aging process at the 0~1000 h aging process. The enrichment of Cr element occurs when the thermal aging time reaches 3000 h, and the Cr element enrichment is significant at 6000 h For the #2 sample, the segregation of Cr element is not significant during the thermal aging process from 0~500 h, and the Cr enrichment occurred when the aging time reached 1000 h By the time of 6000 h, the Cr element segregation in #2 sample is more significant than #1 sample. A locally enlarged TEM image of the ferrite region in #2 sample thermal aged for 6000 h is shown in Fig. 6(a), a large number of clusters marked by the white circles can be observed. After further enlarging one of the clusters, it can be observed that there are areas with different brightness and dark contrasts (Fig. 6(b)). The EDS mapping results of area of Fig. 6(b) indicate that the bright contrast area is rich in Fe and the dark contrast area is rich in Cr, as seen in Fig. 6(c) and Fig. 6 (d).

Fig. 7 shows the one-dimensional Cr concentration profiles obtained from the EDS mapping results (Fig.5). The concentrations were estimated in every 0.135 nm step. For #1 sample, the mean peak-to-peak amplitude of the concentration fluctuation seems to increase with increasing aging duration, but it is not significant, as shown in Fig. 7(a-c). But for the #2 sample, Fig. 7(d-f) indicate that the wavelength and amplitude of the Cr concentration profile have a significant enhancement with the increase of thermal aging time. By contrast, Cr element

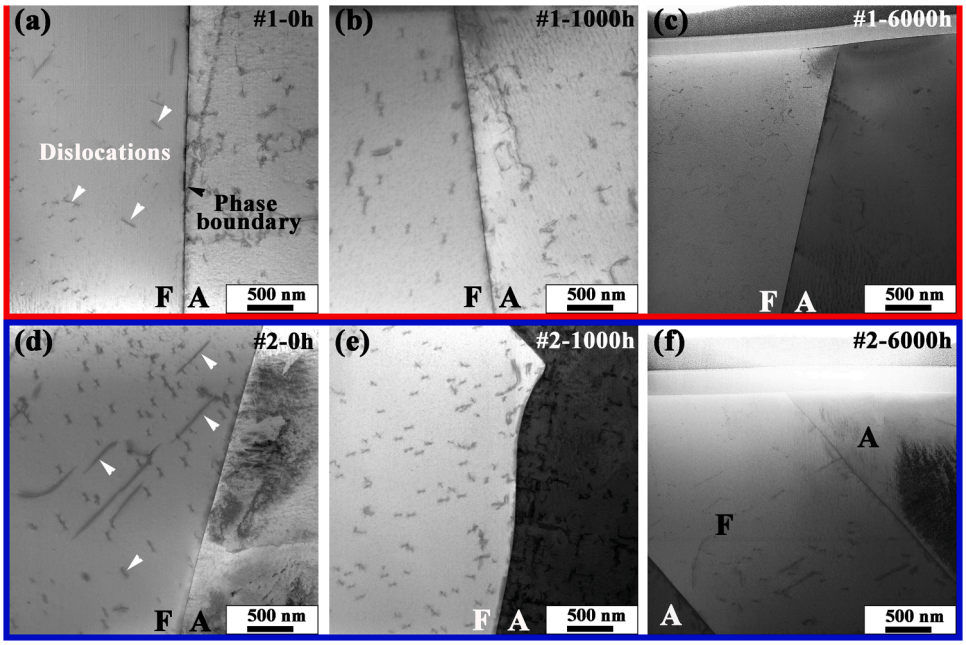

Fig. 4. Overview STEM images of #1 and #2 Z3CN20.09 M CASS alloys under different thermal aging times.

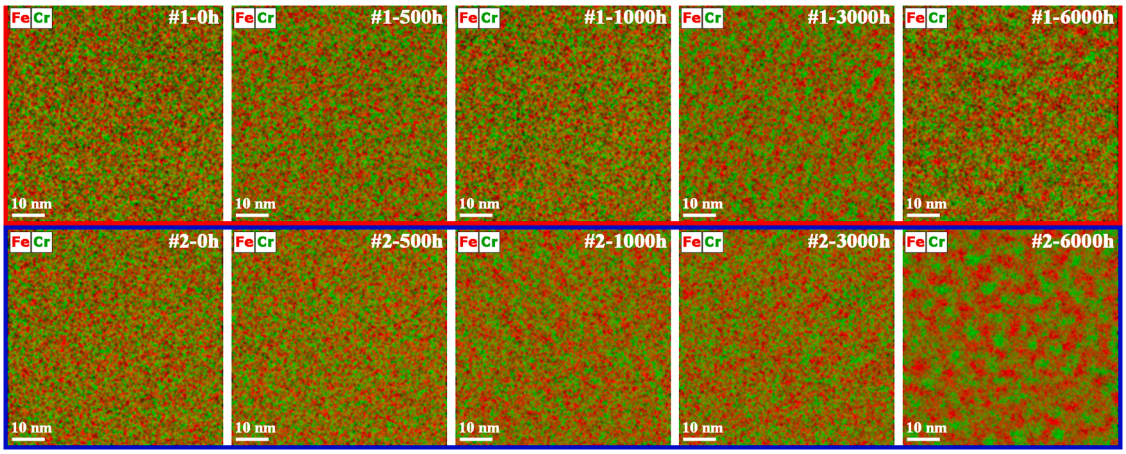

Fig. 5. EDS mapping results for Fe and Cr elements of #1 and #2 Z3CN20.09 M CASS alloys under different thermal aging times.

segregation induced by spinodal decomposition in #2 sample is more significant than that in #1 sample.

4. Discussion

Based on the above experimental results and previous researches [1, 13–25], it can be concluded that with the increase of thermal aging time, the impact toughness of the Z3CN20.09 M CASS alloys material significantly deteriorates, which is mainly related with spinodal decomposition induced element segregation of Fe and Cr. By comparing the experimental results, it can be found that during the thermal aging process, the element segregation in #2 sample is much more significant than that in #1 sample (Figs. 5 and 7). As the size and density of the dislocation defect inside the #2 in the original state are much higher than those in #1 sample (Fig. 4), which always serves as a pathway for the elements diffusion, intensifying the local enrichment of Cr and Fe atoms [46]. And the enriched Cr and Fe clusters can in turn further confine the movement of dislocations defects [47], thereby significantly reducing the mechanical properties. This is also the main reason why the charpy impact energy of #2 sample decreased much faster than that of #1 sample.

According to previous research data and the ANL model that proposed by the U.S.NRC (United States Nuclear Regulatory Commission) [48], Liu [49] proposed a formula to predict the Charpy impact energy (C_v) of Z3CN20.09 M CASS alloys under the thermal aging process, as follows:

$$\lg C_v = logC_{vsat} + \beta \times \left[1 - \tanh\left(\frac{P-\theta}{\alpha}\right)\right], \tag{4}$$

where C_v is the Charpy impact energy; C_{vsat} is the saturated Charpy impact energy, $\log C_{vsat}$=1.97; α=0.98323 is the shape factor of the Charpy-impact energy curve; β=0.2486 is the half the maximum change of the Charpy-impact energy at room temperature; θ=2.9 is the log of the time; P is the thermal aging parameter calculated by the following equation [50]:

$$P(t,T) = \lg t - \frac{1000 \times Q}{19.143} \times \left(\frac{1}{T} - \frac{1}{673}\right), \tag{5}$$

where Q is the activation energy (kJ/mol); t is the thermal aging time

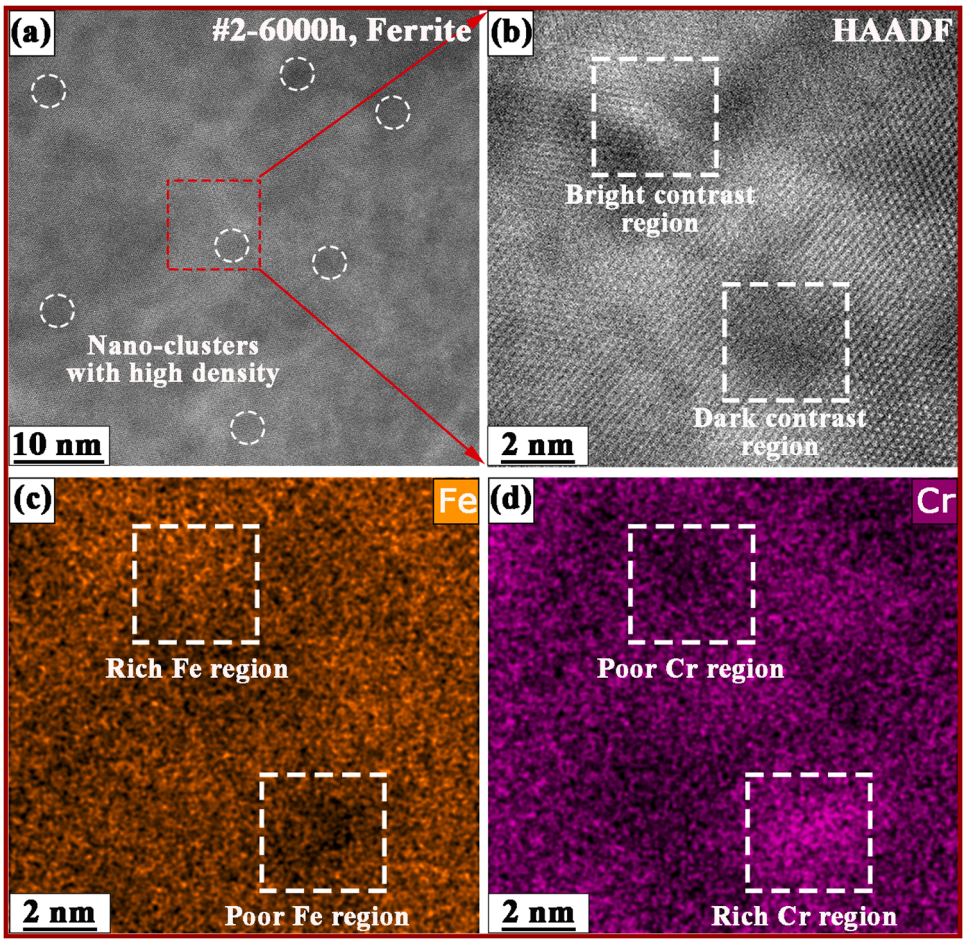

Fig. 6. TEM images with different magnifications and EDS mapping results of #2 samples under 6000 h thermal aging process.

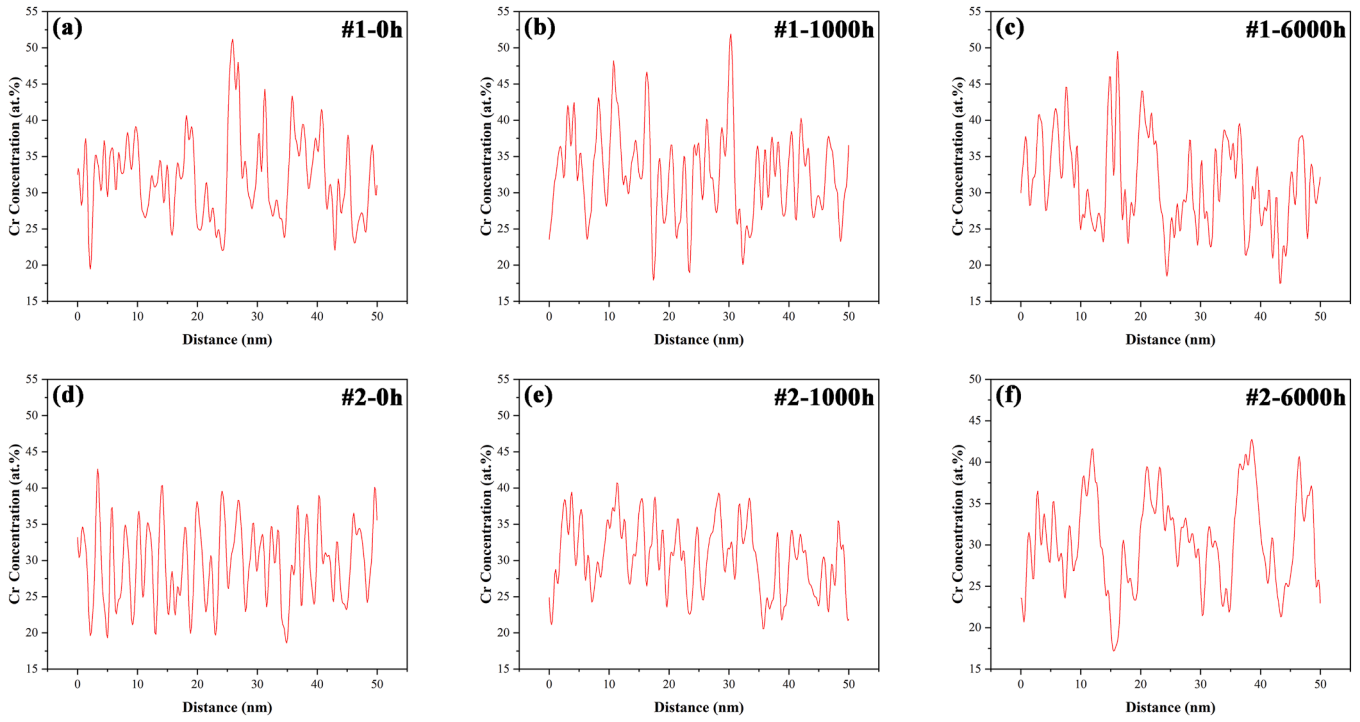

Fig. 7. One-dimensional Cr concentration EDS profiles in the ferrite phase of the #1 and #2 Z3CN20.09 M CASS samples thermally aged at 400 ℃ for different times.

(h); T is the thermal aging temperature (K). However, in this research, the aging temperature is 400℃ (673 K), so $P = \lg t$. The parameters in the ANL model formula were closely related to the specific composition of the material. Thus, based on the actual measured composition data and the Charpy impact energy of the #1 and #2 samples in this research, the relevant parameters were revised. Charpy impact energy data of the samples at each aging time were measured from five samples, and standard deviations were used as the value of error bars. In addition, all the tests were conducted by a third-party testing agency with CNAS qualification. Eventually, the expressions of Charpy impact energy variation with the thermal aging time in this work are:

$$\lg C_v = 1.967280 + 0.300361 \times \left[1 - \tanh\left(\frac{\lg t - \theta_1}{0.978988}\right)\right] \quad (6.1)$$

$$\lg C_v = 1.912012 + 0.284894 \times \left[1 - \tanh\left(\frac{\lg t - \theta_2}{0.935050}\right)\right] \quad (6.2)$$

where θ_1 and θ_2 have an optimal range of values 3.46~3.47 and 3.39~3.48, respectively. The process of thermal aging damage can cause nanoscale migration and aggregation of Fe and Cr atoms in dual phase steel, resulting in changes in the coordination environment around Fe and Cr atoms. Experimental methods such as EDS mapping and atom probe tomography equipped with element quantification functions are often used to describe the micro-element segregation phenomenon inside materials [14,51,52]. However, there is a certain degree of error in the proportion of element components measured by these experimental methods. And due to the small observation area, it is difficult to have statistical significance. Thus, the changes in atomic arrangement can be quantitatively calculated by defining a short-range-order parameter (SRO). Using the Warren-Crowley SRO definition to calculate the atomic scale structural characteristics of Fe-Cr alloys [53], as the following form:

$$\alpha_{Cr}^{k} = 1 - \frac{z_{Fe}^{k}}{z_{tot}^{k}(1 - c_{Cr})}, \quad (7)$$

where α_{Cr}^{k} is the SRO of the k-th shell around Cr atoms; Z_{Fe}^{k}/Z_{tot}^{k} is the percentage of Fe atoms in the k_{th} shell around Cr atoms; c_{Cr} is the concentration of global Cr atoms, α_{Cr}^{k}=0 represents that the concentration of Fe in the vicinity of Cr atoms is consistent with the global Fe concentration, indicating that the alloy is in a solid solution state; α_{Cr}^{k}→1 means that the Cr atoms in the neighborhood are in a phase separation state. In this research, $k = 1$, the concentration of Cr atoms within the first nearest neighbor was statistically analyzed.

The simulation results of the SRO are shown in Fig. 8. The evolution of SRO concerning the Fe and Cr atoms was calculated using simulation boxes of varying sizes. After adjusting for the different vacancy concentrations, the trends from all simulations consistently converged, thereby validating the reliability of the current model. At the initial stage, the SRO was approximately zero, indicating that the distribution of Fe and Cr atoms was nearly uniform. As the aging time increased, the SRO raised and approached an upper limit, suggesting that local clustering of Fe and Cr atoms occurred and eventually reached a saturation state. The subfigures in Fig. 8 depict the distribution of Cr atom clusters at various aging times, illustrating the spatial aggregation patterns as the system evolves. The SRO simulation results are consistent with the enrichment trend of Cr element obtained by EDS characterization (Figs. 5 and 7).

In this work, the SRO of Cr atoms (S_{Cr}) is considered a function of thermal aging time under the condition that the aging temperature and alloy composition remain unchanged. The fitting formula between S_{Cr} and thermal aging time (t) is shown as follows:

$$S_{Cr}^{-1}(t) = S_{MAX}^{-1} + (Ht)^{-1} \quad (8)$$

$$\lg t = -\lg H - \lg\left(S_{Cr}^{-1} - S_{MAX}^{-1}\right), \quad (9)$$

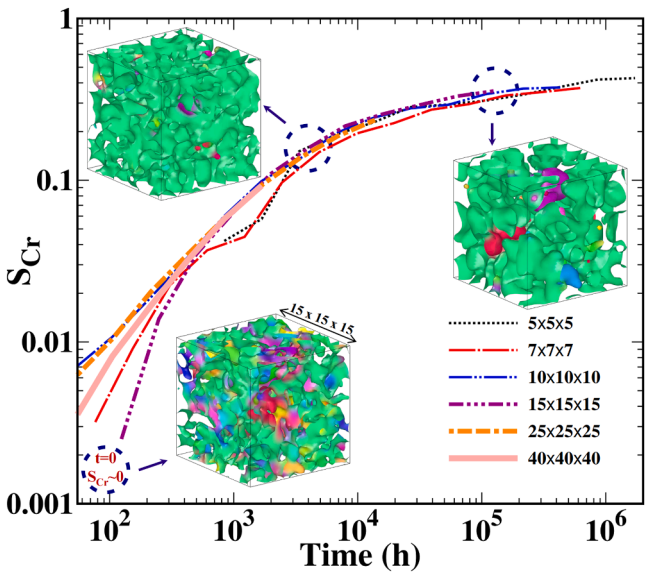

Fig. 8. The variation of SRO of Cr atoms within different sized crystal cells simulated by MC with time steps. The distribution of Cr atom clusters with from the solid solution state to the phase decomposition is attached (cell size: 15×15×15 a_0^3).

where S_{MAX} represents the maximum value of S_{Cr} in the system at thermal equilibrium (t→∞), and H is the growth rate of S_{Cr} over time. The larger the H parameter is, the faster the SRO reaches saturation. The simulated results of the Eqs. (8) and (9) are shown in Fig. 9. The simulation results from sizes 10 to 40 conform to Eqs. (8) and (9), with consistent trends and numerical values. However, results from sizes 5 and 7 exhibited insufficient linearity due to the smaller spatial atomic distribution randomness. Taking into account both computational accuracy and efficiency, a box with a size of 15×15×15 a_0^3 was adopted as the basis for connecting the SRO and aging time and applied in estimating the quantitative relationship between the impact energy and the SRO parameter.

Therefore, the quantitative relationship model between impact energy (C_v) and S_{Cr} at 673 K can be obtained by considering **Eqs. 6** and 9, as shown in the following **Eq. 10**.

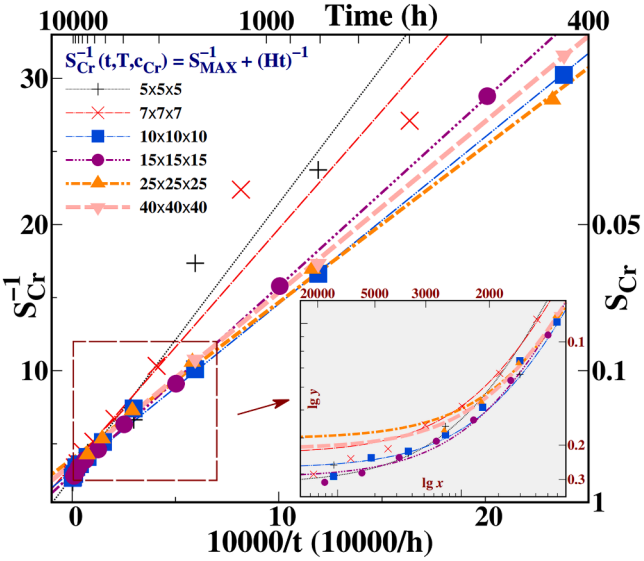

Fig. 9. Linear relationship between the reciprocal of S_{Cr} and the reciprocal of thermal aging time.

$$\lg C_v = 1.967280 + 0.300361 \times \left[1 - \tanh\left(\frac{-lgH - \lg\left(S_{Cr}^{-1} - S_{MAX}^{-1}\right) - \theta_1}{0.978988}\right)\right] \quad (10.1)$$

$$\lg C_v = 1.912012 + 0.284894 \times \left[1 - \tanh\left(\frac{-lgH - \lg\left(S_{Cr}^{-1} - S_{MAX}^{-1}\right) - \theta_2}{0.935050}\right)\right] \quad (10.2)$$

According to thermodynamics and limits of the functions, there is a lower limit for impact energy and an upper limit for S_{Cr} under long-term thermal aging experimental conditions, which can be seen in Fig. 10. The impact energy and S_{Cr} exhibit a strong mathematical correlation, with the variation in S_{Cr} closely mirroring the rate of change in impact energy. Consequently, S_{Cr} serves as an effective indicator for impact energy, which has a prediction accuracy of over 90 % for the mechanical properties of the Z3CN20.09 M cast austenitic stainless steels. Overall, our model fits the experimental data well and has the power to predict the lifetime of the pipeline materials, which has important reference and guidance significance for the life prediction and mechanical performance degradation assessment of reactor structural materials, especially the duplex steel structural components.

5. Conclusions

A quantitative mathematical model has been introduced to establish the relationship between thermal aging defects and mechanical properties for the Z3CN20.09 M cast austenitic stainless steels, which is used as the materials for the main pipeline of the reactor primary circuit. Accelerated thermal aging experiment for two kinds of Z3CN20.09 M cast austenitic stainless steels (#1–Made in France and #2–Made in China) was conducted at 400 ℃.

Short range segregation characteristic structures of Fe and Cr elements induced by spinodal decomposition both appeared inside the samples with the increasing thermal aging time. Thus, the short-range order parameter of the Cr element segregation was chosen as the characteristic defect parameter (S_{Cr}). In all mechanical performance tests, the Charpy impact energy shows a good monotonic decreasing trend with thermal aging time. Thus, Charpy impact energy was used as a characteristic mechanical parameter (C_v). The mechanical model has a prediction accuracy of over 90 % for the mechanical properties of the Z3CN20.09 M cast austenitic stainless steels.

With experimental validation, our model quantitatively correlates the macroscopic mechanical properties and the microscopic thermal aging defects, which has important reference and guidance significance for the life prediction and mechanical performance degradation assessment of reactor structural materials, especially the duplex steel structural components.

CRediT authorship contribution statement

Chao Ye: Writing – review & editing, Writing – original draft, Supervision, Project administration, Investigation, Funding acquisition, Formal analysis, Data curation, Conceptualization. **Ni Jiang:** Writing – original draft, Formal analysis. **Jiannan Hao:** Writing – original draft, Validation, Software. **Xinjie Ma:** Software. **Huiping Liu:** Formal analysis, Investigation. **Jiao Luo:** Supervision, Project administration. **Penghui Lei:** Data curation. **Fangjie Shi:** Investigation, Formal analysis, Data curation. **Qianwu Li:** Investigation, Formal analysis, Data curation. **Yuhua Hang:** Investigation, Data curation. **Pan Qi:** Supervision. **Qing Peng:** Writing – review & editing, Supervision, Investigation.

Declaration of competing interest

The corresponding author and other co-authors have no conflict of interest. And I take complete responsibility for the integrity of the data and the accuracy of the data analysis.

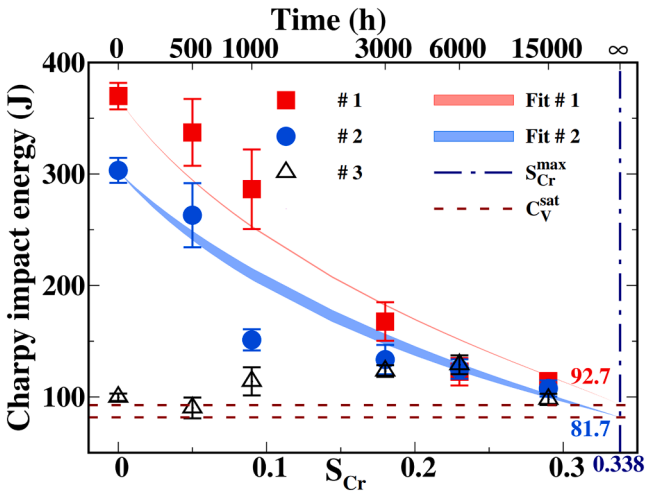

Fig. 10. The limit relationship between impact energy and S_{Cr}.

Acknowledgments

The authors acknowledge the financial support from the National Key R&D Program of China (Grant No. 2022YFB3707200), the National Natural Science Foundation of China (No. 12205236, 12272378), the Strategic Priority Research Program of Chinese Academy of Sciences (Grant No. XDB0620103), and the High-level Innovation Research Institute Program of Guangdong Province (Grant No. 2020B0909010003).

Data availability

The data that has been used is confidential.

References

[1] Y.H. Yao, J.F. Wei, Z.P. Wang, Effect of long-term thermal aging on the mechanical properties of casting duplex stainless steels, Mat. Sci. Eng. A 551 (2012) 116–121, https://doi.org/10.1016/j.msea.2012.04.105.
[2] T.H. Liu, W. Wang, W.J. Qiang, G.G. Shu, Mechanical properties and eddy current testing of thermally aged Z3CN20.09M cast duplex stainless steel, J. Nucl. Mater. 501 (2018) 1–7, https://doi.org/10.1016/j.jnucmat.2018.01.028.
[3] M.Y. Fan, W.Q. Jia, W.W. Yu, D.Y. Wang, M. Guan, Y. Cao, F. Xue, Y.L. Liu, J. W. Yao, B. Lin, T. Yu, Effect of multiple heat treatments on fracture property of centrifugal casting stainless steels Z3CN20.09M with long-term thermal aging degradation, J. Iron Steel Res. Int. 28 (2021) 223–231, https://doi.org/10.1007/s42243-020-00470-5.
[4] B. Zhang, F. Xue, S.L. Li, X.T. Wang, N.N. Liang, Y.H. Zhao, G. Sha, Non-uniform phase separation in ferrite of a duplex stainless steel, Acta Mater 140 (2017) 388–397, https://doi.org/10.1016/j.actamat.2017.08.044.
[5] Y. You, Y.F. Chen, B. Yang, Passive film properties of Z3CN20.09M duplex stainless steel aged for different times, Mater. Corros. 69 (2018) 1205–1217, https://doi.org/10.1002/maco.201709984.
[6] Y. Chen, B. Chen, F. Dong, B. Yang, S. Li, X. Yu, Pitting behavior of thermally aged Z3CN20.09M cast stainless steel for primary coolant pipe of nuclear power plant, Eng. Fail. Anal. 83 (2018) 1–8, https://doi.org/10.1016/j.engfailanal.2017.09.005.
[7] Y. Chen, B. Alexandreanu, W.-Y. Chen, K. Natesan, Z. Li, Y. Yang, A.S. Rao, Cracking behavior of thermally aged and irradiated CF-8 cast austenitic stainless steel, J. Nucl. Mater. 466 (2015) 560–568, https://doi.org/10.1016/j.jnucmat.2015.08.047.
[8] S.A. Dajani, B.R. Dacus, C.A. Dennett, M.G. Burke, L. Waldron, T.S. Byun, J.J. Wall, K.B. Anglin, O.A. Dajani, K.J. Krakowiak, F.-J. Ulm, A. Schwartzmann, C.C. Tasan, P. Hosemann, M.P. Short, Detecting thermally-induced spinodal decomposition with picosecond ultrasonics in cast austenitic stainless steels, Acta Mater. 246 (2023) 118552, https://doi.org/10.1016/j.actamat.2022.118552.
[9] H. Pommier, E.P. Busso, T.F. Morgeneyer, A. Pineau, Intergranular damage during stress relaxation in AISI 316L-type austenitic stainless steels: effect of carbon, nitrogen and phosphorus contents, Acta Mater. 103 (2016) 893–908, https://doi.org/10.1016/j.actamat.2015.11.004.

[10] C. Liu, B.B. Li, Y.B. Cai, X. Chen, Fatigue crack propagation behaviour of pressurised elbow pipes under cyclic bending, Thin Wall. Struct. 154 (2020) 10688, https://doi.org/10.1016/j.tws.2020.106882.
[11] S.L. Li, Y.L. Wang, H.L. Zhang, S.X. Li, K. Zheng, F. Xue, X.T. Wang, Microstructure evolution and impact fracture behaviors of Z3CN20-09M stainless steels after long-term thermal aging, J. Nucl. Mater. 433 (2013) 41–49, https://doi.org/10.1016/j.jnucmat.2012.09.004.
[12] X.F. Chen, D.H. Tian, L.G. Ling, T.G. Liu, H. Wang, Y.Q. Chen, Y.H. Lu, Microstructure and corrosion resistance of Z3CN20.09M stainless steels after different thermo-mechanical processing, J. Nucl. Mater. 577 (2023) 154300, https://doi.org/10.1016/j.jnucmat.2023.154300.
[13] Y. Wang, Y.H. Yao n, Z.P. Wang, Y.H. Jin, X.L. Zhang, J.N. Liu, Thermal ageing on the deformation and fracture mechanisms of a duplex stainless steel by quasi in-situ tensile test under OM and SEM, Mat. Sci. Eng. A 666 (2016) 184–190, https://doi.org/10.1016/j.msea.2016.04.051.
[14] Y. Fan, T.G. Liu, L. Xin, Y.M. Han, Y.H. Lu, T. Shoji, Thermal aging behaviors of duplex stainless steels used in nuclear power plant: a review, J. Nucl. Mater. 544 (2021) 152693, https://doi.org/10.1016/j.jnucmat.2020.152693.
[15] S. Chen, Y. Miyahara, A. Nomoto, K. Nishida, Effects of thermal aging and low-fluence neutron irradiation on the mechanical property and microstructure of ferrite in cast austenitic stainless steels, Acta Mater. 179 (2019) 61–69, https://doi.org/10.1016/j.actamat.2019.08.029.
[16] S.L. Li, Y.L. Wang, S.X. Li, H.L. Zhang, F. Xue, X.T. Wang, Microstructures and mechanical properties of cast austenite stainless steels after long-term thermal aging at low temperature, Mater. Design 50 (2013) 886–892, https://doi.org/10.1016/j.matdes.2013.02.061.
[17] J.D. Tucker, M.K. Miller, G.A. Young, Assessment of thermal embrittlement in duplex stainless steels 2003 and 2205 for nuclear power applications, Acta Mater. 87 (2015) 15–24, https://doi.org/10.1016/j.actamat.2014.12.012.
[18] D. Yu, C. Guo, S. Fu, Y. Chen, K. An, W. Yu, X. Chen, Probing the fatigue enhancement in a thermally aged cast duplex stainless steel by in situ neutron diffraction, Scripta Mater. 252 (2024) 116252, https://doi.org/10.1016/j.scriptamat.2024.116252.
[19] Q. Zhou, L. Cong, L. Gan, C. Ling, D. Li, E.P. Busso, Effect of thermal ageing on the deformation behaviour of ferrite and austenite in a duplex stainless steel: micropillar characterisation and dislocation density modelling, Acta Mater. 265 (2024) 119599, https://doi.org/10.1016/j.actamat.2023.119599.
[20] T.G. Lach, D.A. Collins, T.S. Byun, Evolution of the role of molybdenum in duplex stainless steels during thermal aging: from enhancing spinodal decomposition to forming heterogeneous precipitates, J. Nucl. Mater. 557 (2021) 153268, https://doi.org/10.1016/j.jnucmat.2021.153268.
[21] A. Takahashi, T. Suzuki, A. Nomoto, T. Kumagai, Influence of spinodal decomposition structures on the strength of Fe-Cr alloys: a dislocation dynamics study, Acta Mater. 146 (2018) 160–170, https://doi.org/10.1016/j.actamat.2017.12.051.
[22] Y. Matsukawa, T. Takeuchi, Y. Kakubo, T. Suzudo, H. Watanabe, H. Abe, T. Toyama, Y. Nagai, The two-step nucleation of G-phase in ferrite, Acta Mater. 116 (2016) 104–113, https://doi.org/10.1016/j.actamat.2016.06.013.
[23] H.M. Chung, T.R. Leax, Embrittlement of laboratory and reactor aged CF3,CF8, and CF8M duplex stainless steels, Mater. Sci. Technol. 6 (3) (1990) 249–262, https://doi.org/10.1179/mst.1990.6.3.249.
[24] A. Mateo, L. Llanes, M. Anglada, A. Redjaimia, G. Metauer, Characterization of the intermetallic G-phase in an AISI 329 duplex stainless steel, J. Mater. Sci. 32 (17) (1997) 4533–4540. https://link.springer.com/article/10.1023/A:1018669217124.
[25] T.S. Byun, D.A. Collins, T.G. Lach, E.L. Carter, Degradation of impact toughness in cast stainless steels during long-term thermal aging, J. Mater. Sci. 542 (2020) 152524, https://doi.org/10.1016/j.jnucmat.2020.152524.
[26] T.S. Byun, Y. Yang, N.R. Overman, J.T. Busby, Thermal aging phenomena in cast duplex stainless steels, JOM J. Miner. Metal. Mater. Soc. 68 (2) (2016) 507–516, https://doi.org/10.1007/s11837-015-1709-9.
[27] J.J. Shiao, C.H. Tsai, J.J. Kai, J.H. Huang, Aging embrittlement and lattice image analysis in a Fe-Cr-Ni duplex stainless steel aged at 400°C, J. Nucl. Mater. 217 (3) (1994) 269–278, https://doi.org/10.1016/0022-3115(94)90376-X.
[28] S. Li, Y. Wang, X. Wang, Effects of ferrite content on the mechanical properties of thermal aged duplex stainless steels, Mat. Sci. Eng. A 625 (2015) 186–193, https://doi.org/10.1016/j.msea.2014.11.065.
[29] Evaluation of Thermal Aging Embrittlement for Cast Austenitic Stainless Steel Components: EPRI, Palo Alto, CA: 2001. 1000976, https://www.nrc.gov/docs/ML0037/ML003727111.pdf.
[30] J.W. Cahn, On spinodal decomposition, Acta Metallurgica 9 (1961) 795–801, https://doi.org/10.1016/0001-6160(61)90182-1.
[31] J.S. Langer, Theory of spinodal decomposition in alloys, Ann. Phys. 65 (1971) 53–86, https://doi.org/10.1016/0003-4916(71)90162-X.
[32] P. Auger, F. Danoix, A. Menand, S. Bonnet, J. Bourgoin, M. Guttmann, Atom probe and transmission electron microscopy study of aging of cast duplex stainless steels, Mater. Sci. Technol. 6 (1990) 301–313, https://doi.org/10.1179/mst.1990.6.3.301.
[33] S. Lee, P.T. Kuo, K. Wichman, O.K. Chopra, Flaw evaluation of thermally aged cast stainless steel in light-water reactor applications, Int. J. Pres. Ves. Piping 72 (1997) 37–44, https://doi.org/10.1016/S0308-0161(97)00007-0.
[34] O.K. Chora, W.J. Shack, Assessment of thermal embrittlement of cast stainless steels. NUREG/CR-6177. U.S. Nuclear Regulatory Commission, Washington, DC, May 1994, https://doi.org/10.2172/10159200.
[35] Q. Zhang, A.S.S. Singaravelu, Y. Zhao, T. Jinga, N. Chawla, Mechanical properties of a thermally-aged cast duplex stainless steel by nanoindentation and micropillar compression, Mat. Sci. Eng. A 743 (2019) 520–528, https://doi.org/10.1016/j.msea.2018.11.112.
[36] H.M. Chung, Aging and life prediction of cast duplex stainless steel components, Int. J. Pres. Ves. Pip. 50 (1992) 179–213, https://doi.org/10.1016/0308-0161(92)90037-G.
[37] G. Bonny, N. Castin1, J. Bullens, A. Bakaev, T.C.P. Klaver, D. Terentyev, On the mobility of vacancy clusters in reduced activation steels: an atomistic study in the Fe–Cr–W model alloy, J. Phys.: Condens. Matter 25 (2013) 315401, https://doi.org/10.1088/0953-8984/25/31/315401.
[38] S. Plimpton, Fast parallel algorithms for short-range molecular dynamics, J. Comput. Phys. 117 (1) (1995) 1–19, https://doi.org/10.1006/jcph.1995.1039.
[39] N. Metropolis, A.W. Rosenbluth, M.N. Rosenbluth, A.H. Teller, E. Teller, Equation of state calculations by fast computing machines, J. Chem. Phys. 21 (1953) 1087–1092, https://doi.org/10.1007/s12045-022-1419-x.
[40] A.B. Bortz, M.H. Kalos, J.L. Lebowitz, A new algorithm for Monte Carlo simulation of Ising spin systems, J. Comput. Phys. 17 (1) (1975) 10–18, https://doi.org/10.1016/0021-9991(75)90060-1.
[41] J. Hao, S. Jin, G. Lu, H. Xu, Migration energy barriers and diffusion anisotropy of point defects on tungsten surfaces, Comput. Mater. Sci. 184 (2020) 109893, https://doi.org/10.1016/j.commatsci.2020.109893.
[42] L. Malerba, M.C. Marinica, N. Anento, C. Björkas, H. Nguyen, C. Domain, F. Djurabekova, P. Olsson, K. Nordlund, A. Serra, D. Terentyev, F. Willaime, C. S. Becquart, Comparison of empirical interatomic potentials for iron applied to radiation damage studies, J. Nucl. Mater. 406 (1) (2010) 19–38, https://doi.org/10.1016/j.jnucmat.2010.05.017.
[43] F. Shi, N. Li, J. Guo, B. Chen, S. Li, H. Liu, J. Guo, Q. Li, Y. Li, B. Xiao, Monte-Carlo simulation of mass density field coupled dynamics for microstructural evolution of Fe-Cr binary alloys, Acta Phys. Sin. 72 (13) (2023) 136401, https://doi.org/10.7498/aps.72.20230291.
[44] C. Pareige, S. Novy a, S. Saillet, P. Pareige, Study of phase transformation and mechanical properties evolution of duplex stainless steels after long term thermal ageing (>20 years), J. Nucl. Mater. 411 (2011) 90–96, https://doi.org/10.1016/j.jnucmat.2011.01.036.
[45] T.G. Lach, T.S. Byun, K.J. Leonard, Mechanical property degradation and microstructural evolution of cast austenitic stainless steels under short-term thermal aging, J. Nucl. Mater. 497 (2017) 139–153, https://doi.org/10.1016/j.jnucmat.2017.07.059.
[46] X.Y. Cao, P. Zhu, X.F. Ding, Y.H. Lu, T. Shoji, An investigation on microstructure and mechanical property of thermally aged stainless steel weld overlay cladding, J. Nucl. Mater. 486 (2017) 172–182, https://doi.org/10.1016/j.jnucmat.2017.01.019.
[47] Y.-C. Hsieh, L. Zhang, T.-F. Chung, Y.-T. Tsai, J.-R. Yang, T. Ohmura, T. Suzuki, In-situ transmission electron microscopy investigation of the deformation behavior of spinodal nanostructured δ-ferrite in a duplex stainless steel, Scr. Mater. 125 (2016) 44–48, https://doi.org/10.1016/j.scriptamat.2016.06.047.
[48] O.K. Chopra, Estimation of Fracture Toughness of Cast Stainless Steels during Thermal Aging in LWR Systems, NUREG/CR-4513, U.S. Nuclear Regulatory Commission, Washington, 1994, pp 23–29, https://www.nrc.gov/docs/ML1135/ML11356A348.pdf.
[49] T. Liu, W. Wang, W. Qiang, G. Shu, Mechanical properties and kinetics of thermally aged Z3CN20.09M cast duplex stainless steel, Int. J. Min. Met. Mater. 25 (2018) 1148–1155. https://link.springer.com/article/10.1007/s12613-018-1666-8.
[50] T.R. Leax, S.S. Brenner, J.A. Spitznagel, Atom probe examination of thermally ages CF8M cast stainless steel, Metall. Trans. A 23 (1992) 2725–2736. https://link.springer.com/article/10.1007/BF02651752.
[51] J. Zhou, J. Odqvist, M. Thuvander, P. Hedström, Quantitative evaluation of spinodal decomposition in Fe-Cr by atom probe tomography and radial distribution function analysis, Microsc. Microanal. 19 (2013) 665–675, https://doi.org/10.1017/S1431927613000470.
[52] J.H. Jackson, D. Paraventi, M. Wright, Proceedings of the 18th International Conference on Environmental Degradation of Materials in Nuclear Power Systems - Water Reactors, Miner. Metals Mater. Ser. 2019, https://doi.org/10.1007/978-3-030-04639-2.
[53] P. Erhart, A. Caro, M.S. Caro, B. Sadigh, Short-range order and precipitation in Fe-rich Fe–Cr alloys: atomistic off-lattice Monte Carlo simulations, Phys. Rev. B 77 (2008) 134206, https://doi.org/10.1103/PhysRevB.77.134206.